Evoked response activity eigenmode analysis in a convoluted cortex via neural field theory

K. N. Mukta,[1,2,*] P. A. Robinson,[1,2] J. C. Pagès,[1,2,3] N. C. Gabay,[1,2] and Xiao Gao[1,2]
[1]*School of Physics, University of Sydney, New South Wales 2006, Australia*
[2]*Center for Integrative Brain Function, University of Sydney, New South Wales 2006, Australia*
[3]*School of Physics, University of Zurich, Zürich, Canton of Zürich, Switzerland*

(Received 13 December 2019; accepted 15 July 2020; published 8 December 2020)

Neural field theory of the corticothalamic system is used to explore evoked response potentials (ERPs) caused by spatially localized impulse stimuli on the convoluted cortex and on a spherical cortex. Eigenfunctions are calculated analytically on the spherical cortex and numerically on the convoluted cortex via eigenfunction expansions. Eigenmodes on a convoluted cortex are similar to those of the spherical cortex, and a few such modes are found to be sufficient to reproduce the main ERP features. It is found that the ERP peak is stronger in spherical cortex than convoluted cortex, but in both cases the peak decreases monotonically with increasing distance from the stimulus point. In the convoluted case, cortical folding causes ERPs to differ between locations at the same distance from the stimulus point and spherical symmetries are only approximately preserved.

DOI: 10.1103/PhysRevE.102.062303

I. INTRODUCTION

Evoked response potentials (ERPs) occur due to impulse stimuli and these responses are obtained by averaging over many stimuli to improve their signal to noise ratio relative to background electroencephalographic (EEG) activity [1,2]. Neural field theory (NFT) modeling of ERP generation [3,4] has enabled the underlying physiological parameters that correspond to various states to be deduced, and the parameters underlying ERPs to be inferred, from recording from the scalp or within the brain [2–11].

Physiology-based NFT has been successfully used to analyze brain activity from small scales to the whole brain and to examine brain activity in terms of eigenmodes [12,13]. Our prior work [12,14] examined modal effects on white-noise-driven spectra in a planar system. This work found that the modal spectrum is dominated by the contributions from the spatially uniform global mode, which is symmetric between brain hemispheres and approximately uniform across each [15,16]. Our recent work examined cortical modal effects on EEG spectra, correlations, coherence, and evoked response potentials [14,17]. We found that relatively few eigenmodes are needed for an accurate representation of macroscopic brain activity. In these analyses, we used the approximation of spherical geometry to analyze activity in terms of eigenmodes via a corticothalamic model of a single brain hemisphere, using spherical harmonics. Indeed, other recent works showed that the low-order eigenmodes of a single brain hemisphere are close analogs of spherical harmonics [13,18].

Each hemisphere of the brain has a spherical topology and is convoluted rather than being planar or uniformly curved. In this work, we numerically analyze ERPs in the convoluted cortex in which each brain hemisphere is a highly distorted sphere that exhibits numerous sulci (grooves) and gyri (ridges). Much work has been done on brain activity via eigenmode analysis using a spherical model of the skull [16,19], but this work did not consider individual brain hemispheres or the thalamus, as needed for more realistic and general brain models [13,14]. Our recent work showed that just a very few modes could explain experimentally evoked responses to random visual input stimuli [20] and there has been very recent interest in spherical harmonic expansions from other authors [21,22]. Key issues that we explore here are the use of brain activity eigenmodes on a convoluted cortex to represent realistic ERPs and how much difference cortical folding makes.

The structure of this paper is as follows: After briefly reviewing the neural field model of the corticothalamic system and analytical methods for eigenmode activity in the spherical cortex in Sec. II, we discuss numerical methods for eigenmode analysis in the convoluted cortex. In Sec. III, we discuss the ERP time series, modal effects, and numerical analysis for the convoluted cortex. Finally, Sec. IV presents the conclusions.

II. NEURAL FIELD THEORY OF THE CORTICOTHALAMIC SYSTEM

In this section, we start with a brief review of the neural field corticothalamic model that we employ [23–25] and a brief review of the relevant results from our recent work on evoked response potentials on a spherical cortex [17], in which we derived analytical formulas using our corticothalamic neural field model. After that, we numerically calculate evoked response potentials on the convoluted cortex, and the transfer function for neural activity for a single brain hemisphere [14,17,23–25].

A. Neural field theory

The corticothalamic system is chiefly responsible for the generation of observed ERP signals [1,2,26], so we use a recent physiology-based neural field model of activity in this

*Corresponding author, present address: Department of Natural Science, American International University Bangladesh, Dhaka 1229, Bangladesh; muktaphy@gmail.com

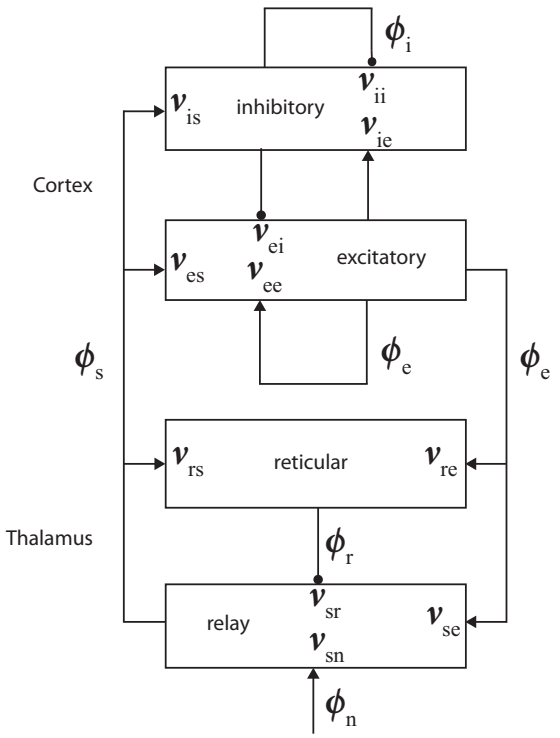

FIG. 1. Schematic diagram of a corticothalamic neural field model of the system. The neural populations shown are cortical excitatory e, cortical inhibitory i, thalamic reticular r, and thalamic relay s. Each parameter ν_{ab} from Eq. (1) quantifies the connection to population a from population b. Excitatory connections are shown with pointed arrowheads and inhibitory connections are shown with round arrowheads.

system to predict and analyze ERPs; such models have been developed and used over several decades [16,24,27–29]. The model used here has been widely employed in previous work [23,24] and incorporates the populations and connections shown in Fig. 1: excitatory (e) and inhibitory (i) cortical neurons, thalamic relay neurons (s), thalamic reticular neurons (r), and sensory inputs (n) [23,30]. The predictions of this model have been verified against many types of EEG phenomena as well as independent physiological measurements [25,31].

The activity in a given population of neurons is determined by the activity of all populations that synapse onto that population, including activity from self-connections. Hence, the net effect P_a on the activity of neurons of population a by all populations of neurons b is given by

$$P_a(\mathbf{r},t) = \sum_b \nu_{ab}\phi_b(\mathbf{r}, t-\tau_{ab}), \tag{1}$$

with [23,24] $\nu_{ab} = s_{ab}N_{ab}$, where N_{ab} is the mean number of synapses to neurons of type a from type b, s_{ab} is the mean time-integrated strength of soma response per incoming spike, ϕ_b is the activity (expressed as the mean rate of action potentials) arising from neurons of type b, τ_{ab} embodies the discrete time delay for signals to propagate to population a from b when these are in different structures, and the sum is over all populations of neurons that have connections to neurons of population a [25,30,32].

The effect of synaptic activity on the mean postsynaptic population's membrane potential involves the kinetics of the neurotransmitter and the electrical properties of dendrites, its receptor, and soma capacitance, all of whose dynamics attenuate high frequency components of the signal. This dynamics can be approximated by the convolution kernel

$$L(t) = \frac{\alpha\beta}{\beta-\alpha}(e^{-\alpha t} - e^{-\beta t}), \tag{2}$$

for $t \geqslant 0$, with $L = 0$ for $t < 0$, where $1/\beta$ and $1/\alpha$ are the rise time and decay time constants, respectively [2,24]. The membrane potential V_a (relative to resting) for a population of neurons is then approximated by a convolution of net activity P_a and this kernel, with

$$V_a(\mathbf{r},t) = \int_{-\infty}^{t} L(t-t')P_a(\mathbf{r},t')dt'. \tag{3}$$

The activity of a population of neurons exhibits a sigmoid response to increasing mean membrane depolarization because its cells have a distribution of the difference between individual soma voltage and threshold potential due to variations in environment and membrane properties. This response is approximated by [2,24,28]

$$Q_a(\mathbf{r},t) = \frac{Q_{\max}}{1+\exp\{-C(V_a-\theta_a)/\sigma_a\}}, \tag{4}$$

where Q_a is the mean firing rates, $Q_{\max}$ is the maximum firing rate, θ_a is the mean neural firing threshold, σ_a is the standard deviation of the difference between individual neuron's soma voltages and threshold, and $C = \pi/\sqrt{3}$.

Treating the EEG signal as being the result of small perturbations about a steady state, the response function becomes [2,33]

$$Q_a(\mathbf{r},t) \approx Q_a^{(0)} + \rho_a\left[V_a(\mathbf{r},t) - V_a^{(0)}\right], \tag{5}$$

where

$$\rho_a \equiv \frac{dQ_a}{dV_a} = \frac{CQ_a}{\sigma_a}\left(1 - \frac{Q_a}{Q_a^{\max}}\right), \tag{6}$$

evaluated at the steady state. It is not necessary to determine the steady state firing rate $Q_a^{(0)}$ because only perturbations to this value are used in the model. Henceforth, to avoid unduly cumbersome notation, the quantities Q_a, ϕ_a, and V_a denote perturbations from their fixed points.

To relate the neuronal activity ϕ_a to the average membrane potential Q_a, we use a damped wave equation to approximate the propagation of neuronal activity in the cortex [12,23,24]. Hence,

$$D_\alpha\phi_a(\mathbf{r},t) = Q_a(\mathbf{r},t), \tag{7}$$

$$D_\alpha = \frac{1}{\gamma_a^2}\left[\frac{\partial^2}{\partial t^2} + 2\gamma_a\frac{\partial}{\partial t} + \gamma_a^2 - v_a^2\nabla^2\right], \tag{8}$$

where $\gamma_a = v_a r_a$ is the temporal damping rate, v_a is the axonal propagation velocity, and r_a is the characteristic range of axons for neurons of population a [24]. Since cortical inhibitory neurons have short ($\sim 10^{-4}$ m) axons, we assume $r_i \approx 0$, and hence $D_i \approx 1$ [24]; the same approximation can be made for intrathalamic connections, so $D_s \approx D_r \approx 1$ [2].

To obtain the transfer function, we first Fourier transform Eqs. (2)–(6). We define the Fourier transform of a function $g(t)$ via the convention

$$g(\omega) = \int_{-\infty}^{\infty} g(t) e^{i\omega t} dt. \tag{9}$$

Assuming that a signal traveling from the thalamus to cortex, or vice versa, takes a time $t_0/2$, so $\tau_{es} = \tau_{se} = \tau_{re} = t_0/2$, and all other τ_{ab} are zero, we find that Eq. (2) becomes

$$P_e(\mathbf{k}, \omega) = \nu_{ee}\phi_e + \nu_{ei}\phi_i + \nu_{es} e^{i\omega t_0/2}\phi_s, \tag{10}$$

$$P_i(\mathbf{k}, \omega) = \nu_{ii}\phi_i + \nu_{ie}\phi_e + \nu_{is} e^{i\omega t_0/2}\phi_s, \tag{11}$$

$$P_s(\mathbf{k}, \omega) = \nu_{se}\phi_e e^{i\omega t_0/2} + \nu_{sr}\phi_r + \nu_{sn}\phi_n, \tag{12}$$

$$P_r(\mathbf{k}, \omega) = \nu_{re}\phi_e e^{i\omega t_0/2} + \nu_{rs}\phi_s, \tag{13}$$

where $\mathbf{k}$ is the wave number and ω is the frequency. Equations (3)–(5), and (7) then become

$$L(\omega) = \left(1 - \frac{i\omega}{\beta}\right)^{-1}\left(1 - \frac{i\omega}{\alpha}\right)^{-1}, \tag{14}$$

$$V_a(\mathbf{k}, \omega) = L(\omega) P_a(\mathbf{k}, \omega), \tag{15}$$

$$Q_a(\mathbf{k}, \omega) = \rho_a V_a(\mathbf{k}, \omega), \tag{16}$$

$$D_a(\mathbf{k}, \omega)\phi_a(\mathbf{k}, \omega) = Q_a(\mathbf{k}, \omega), \tag{17}$$

$$D_e(\mathbf{k}, \omega) = k^2 r_e^2 + (1 - i\omega/\gamma_e)^2, \tag{18}$$

$$D_i = D_s = D_r = 1. \tag{19}$$

B. Transfer function

The scalp potential measured using EEG techniques is directly related to ϕ_e [2,15,16] and the stimulus is written as ϕ_n. To determine the evoked activity from a stimulus ϕ_n requires the transfer function ϕ_e/ϕ_n, which is the cortical excitatory response per unit of external stimulus, including the relative phase [23], and is found by eliminating the P_a, V_a, and Q_a from Eqs. (10)–(19). Assuming the observed random cortical connectivity [34], we make the approximation that $G_{ab} = G_{cb}$ for all $a, c = e, i$ and all $b = e, i, s$ [2]. The transfer function for an impulse traveling directly from the thalamus to the cortex is then given by [2,33]

$$T_{en}(\mathbf{k}, \omega) = \frac{\phi_e(\mathbf{k}, \omega)}{\phi_n(\mathbf{k}, \omega)} \tag{20}$$

$$= \frac{\mathcal{I}}{\mathcal{M}_c - \mathcal{M}_t}, \tag{21}$$

with

$$\mathcal{I} = \frac{e^{i\omega t_0/2} L^2 G_{esn}}{1 - L^2 G_{srs}}, \tag{22}$$

and where the modulation of this signal by cortical feedback is

$$\mathcal{M}_c = D_e(1 - LG_{ei}) - LG_{ee}, \tag{23}$$

and the modulation by corticothalamic loops is

$$\mathcal{M}_t = \frac{e^{i\omega t_0}(L^2 G_{ese} + L^3 G_{esre})}{1 - L^2 G_{srs}}, \tag{24}$$

where G_{ab} is the net gain of two or more populations,

$$G_{ab} = \frac{\partial Q_a}{\partial Q_b} = \rho_a N_{ab} s_b = \rho_a \nu_{ab}, \tag{25}$$

with the derivative evaluated at the fixed point. The net gain of more than two populations of neurons connected serially is simply the product of the separate gains, and we write such compound gains as $G_{ab}G_{bc} = G_{abc}$, for example. In the reduced model, the five relevant linear gains that result are G_{ee}, G_{ei}, G_{ese}, G_{esre}, and G_{srs}. Each of these is the ratio of the change in the activity of neurons of population a in response to a unit change in the incoming activity from neurons of population b.

C. Analytic calculation of ERPs

In our recent work, we derived analytical formulas for ERPs in a spherical brain geometry. Here we outline the derivation of the transfer function for an impulse stimuli. In our prior work [14,17] using our corticothalamic neural field theory, we calculate transfer functions as a ratio of the cortical excitatory response ϕ_e to external stimuli ϕ_n. We can write the transfer function as [14,17]

$$T(\mathbf{k}, \omega) = \frac{A(\omega)}{k^2 r_e^2 + q^2 r_e^2}, \tag{26}$$

where

$$A(\omega) = \frac{e^{i\omega t_0/2} L^2 G_{esn}}{(1 - L^2 G_{srs})(1 - G_{ei}L)}, \tag{27}$$

with

$$q^2 r_e^2 = \left(1 - \frac{i\omega}{\gamma_e}\right)^2 - \frac{1}{1 - G_{ei}L} \times \left\{LG_{ee} + \frac{[L^2 G_{ese} + L^3 G_{erse}]e^{i\omega t_0}}{1 - L^2 G_{srs}}\right\}. \tag{28}$$

By solving the Helmholtz equation on a cortical hemisphere, one can obtain NFT eigenvalues (k_η^2) and eigenmodes η [13,14,17,18,20]. Then for an eigenvalue k_η^2, we can write the corresponding contribution to the transfer function as

$$T\left(k_\eta^2, \omega\right) = \frac{A(\omega)}{k_\eta^2 r_e^2 + q^2 r_e^2}. \tag{29}$$

If one approximates a brain hemisphere as a sphere of radius R_s, the eigenmodes are

$$y_{\ell m}(\vartheta, \varphi) = Y_{\ell m}(\vartheta, \varphi), \tag{30}$$

where η has been replaced by ℓm, the $Y_{\ell m}$ are the real spherical harmonics [14,17], and

$$k_{\ell m}^2 r_e^2 = \frac{r_e^2}{R_s^2}\ell(\ell + 1). \tag{31}$$

In this case, the eigenvalues depend only on the angular momentum mode number $\ell = 0, 1, \ldots$ and are independent of the azimuthal mode number $m = -\ell, \ldots, \ell$.

In our recent work [17], we derived the form of the ERPs by considering an impulselike stimulus $\phi_n(\vartheta, \varphi, t)$ to be approximately Gaussian in both space and time, with the form

$$\phi_n(\vartheta, \varphi, t) = \frac{\mathcal{D}}{t_s\sqrt{2\pi}}\exp\left\{-\frac{1}{2}\left(\frac{t-t_{os}}{t_s}\right)^2\right\}\exp\left(\frac{\cos\vartheta}{\theta_s}\right), \quad (32)$$

with $\mathcal{D} = [4\pi\theta_s^2\sinh(\theta_s^{-2})]^{-1}$ normalizing the stimulus to have unit integral. Here, t_s is the characteristic duration of the stimulus, t_{os} is the stimulus onset time, and θ_s is the angular width of the stimulus. When modeling impulsive stimuli, t_s and θ_s are small, in which case $\cos(\vartheta/\theta_s) \approx 1 - \vartheta^2/2\theta_s^2$, from whence the profile in Eq. (12) is approximately Gaussian at small ϑ.

After spherical harmonic transformation and a Fourier transformation with respect to time t, Eq. (32) yields [17]

$$\phi_n(\ell, m, \omega) = \frac{1}{2\sqrt{2}\theta_s\sinh\left(\theta_s^{-2}\right)}\exp\left(-\frac{1}{2}\omega^2 t_s^2\right)\exp(i\omega t_{os}) \times \sqrt{2\ell+1}I_{\ell+1/2}\left(\frac{1}{\theta_s^2}\right). \quad (33)$$

Finally, to calculate the response ϕ_e evoked by a change in the input stimulus ϕ_n, we inverse Fourier transform to the time domain, giving

$$R(\vartheta, \varphi, t) = \frac{1}{2\pi R_s^2}\sum_{\ell=0}^{\infty}\sum_{m=-\ell}^{\ell}\int T(\ell, m, \omega)\phi_n(\ell, m, \omega) \times Y_{\ell m}(\vartheta, \varphi)e^{-i\omega t}d\omega. \quad (34)$$

D. Numerical calculation of ERPs

To provide the background to our numerical methods, we first outline how activity can be decomposed into eigenmodes and eigenfunctions [35,36]. The linear response in $\phi(\mathbf{r}, t)$ is to be calculated after an impulse stimulus $\phi_n(\mathbf{r}, t)$, where $\mathbf{r}$ and t are the spatial and temporal coordinates on the cortex. After Fourier transform vs t, we express $\phi_n(\mathbf{r}, \omega)$ in terms of eigenfunction decomposition, with

$$\phi_n(k_\eta, \omega) = \int \phi_n(\mathbf{r}, \omega)y(k_\eta)dS, \quad (35)$$

where dS denotes a surface element of the cortical hemisphere; this is parallel to Eq. (34) in [17]. In this paper, we compute the activity ϕ_e evoked by a stimulus that is a δ function at a position $\mathbf{r}_0$ and Gaussian in time. Such a stimulus has the normalized form [2]

$$\phi_n(\mathbf{r}, t) = \delta(\mathbf{r} - \mathbf{r}_0)\frac{1}{t_s\sqrt{2\pi}}\exp\left[-\frac{1}{2}\left(\frac{t-t_{os}}{t_s}\right)^2\right], \quad (36)$$

and after Fourier transforming vs t, we obtain

$$\phi_n(\mathbf{r}, \omega) = \delta(\mathbf{r} - \mathbf{r}_0)e^{i\omega t_{os}}e^{-\frac{1}{2}\omega^2 t_s^2}. \quad (37)$$

For numerical analysis, we discretize the cortical surface using the FREESURFER cortical surface with $N_p = 163\,892$ points [37]. To parametrize the surface, we map every point on a convoluted cortical hemisphere to a point on a sphere using the one-to-one mapping defined in the FREESURFER software. This is shown in Fig. 2, where we see that each point $\mathbf{r}(\vartheta, \varphi)$ of the original cortex on the hemisphere is mapped to ϑ and φ on the sphere, and vice versa. We set the areas of the convoluted cortex and spherical cortex to be equal by setting R_s so that $4\pi R_s^2 = A_{\text{tot}}$, where $A_{\text{tot}} = 0.0616\ \text{m}^2$ is the total area of the cortical hemisphere computed from the FREESURFER discretized grid; this yields $R_s = 0.07$ m.

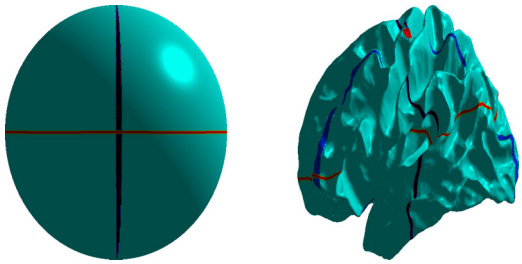

FIG. 2. Equivalence of coordinates on inflated sphere and original cortex. The pole ($\vartheta = 0$) is denoted by a red dot, the equator ($\vartheta = \pi/2$) by a red line, the black line corresponds to $\varphi = \pi/2$ and the blue line to $\varphi = \pi/2$, or $\varphi = 3\pi/2$.

The total transfer function summed over spatial modes is the system response to an impulse stimulus. The eigenfunctions are calculated numerically using the Helmholtz equation, as discussed in [14], but the sum over eigenmodes is the same as in the analytical case above. We compute the surface structure, eigenmodes, and eigenvalues using the FREESURFER surface file [37] via finite element methods (FEM) as in [20]. The transfer function $T(k_\eta, \omega)$ is then computed from Eq. (29) for eigenvalues k_η and frequencies ω_η using the physiological parameters shown in Table I and Eqs. (34)–(38). The transfer function T is computed using the physiological parameters shown in Table I. So to calculate the response $\phi_e(\mathbf{r}, t)$, we must inverse Fourier transform the product of Eqs. (29) and (35). So after multiplying Eq. (35)

TABLE I. Nominal corticothalamic model parameter values from recent work [17], where the first column shows the symbol for the quantity in the second column. The third and fourth columns show the values of the quantity and its units, respectively.

Symbol	Quantity	Value	Unit
α	Synaptodendritic decay rate	45	s^{-1}
β	Synaptodendritic rise rate	185	s^{-1}
t_0	Corticothalamic loop delay	0.085	s
γ_e	Cortical damping rate	116	s^{-1}
r_e	Excitatory axon range	0.086	m
G_{ee}	Excitatory cortical gain	15	
G_{ii}	Inhibitory cortical gain	−17.5	
G_{ese}	Excitatory cortical gain	12.3	
G_{esre}	Excitatory inhibitory gain	−13.0	
G_{srs}	Intrathalamic gain	−0.7	
R_s	Radius of sphere	0.07	m
θ_s	Width of the stimulus	0.3°	
t_{os}	Stimulus onset	0.5	s
t_s	Stimulus duration	0.019	s

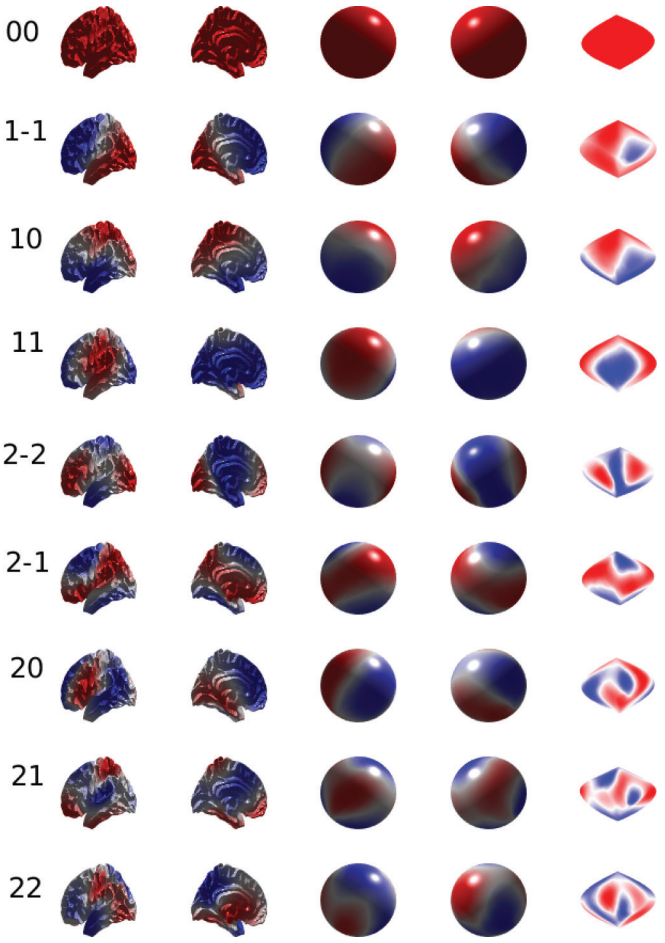

FIG. 3. NFT eigenmodes of the single brain hemisphere on a convoluted cortex for the mode numbers $\lambda\mu$ shown to the left of the first column. Red indicates positive eigenmode regions and blue indicates negative eigenmode regions. Nodal lines are shown in white. The first and second columns show lateral and medial views on the convoluted cortical hemisphere. The third and fourth columns show the same views, but with the hemisphere projected onto a sphere. The fifth column shows a flattened projection of the modes so the whole surface is visible in a single view.

by $T(k_\eta, \omega)$, we obtain

$$\phi_e(\mathbf{r}, \omega) = \sum_\eta y_\eta(\mathbf{r})\phi_e(k_\eta, \omega), \tag{38}$$

which is the convoluted cortex equivalent of Eqs. (36), (43), and (65) in [17] for infinite planar geometry, finite two-dimensional (2D) cortex, and spherical geometry, respectively.

Finally, we compute the evoked response activity ϕ_e for stimuli $\phi_n(\mathbf{k}, \omega)$ at a given position in the cortex via the inverse Fourier transform of Eq. (38),

$$\phi_e(\mathbf{r}, t) = \sum_\eta y_\eta(\mathbf{r}) \int e^{-i\omega t}\phi_e(k_\eta, \omega)d\omega \tag{39}$$

$$= \sum_\eta y_\eta(\mathbf{r}) \int e^{-i\omega t}T(k_\eta, \omega)\phi_n(k_\eta, \omega)d\omega, \tag{40}$$

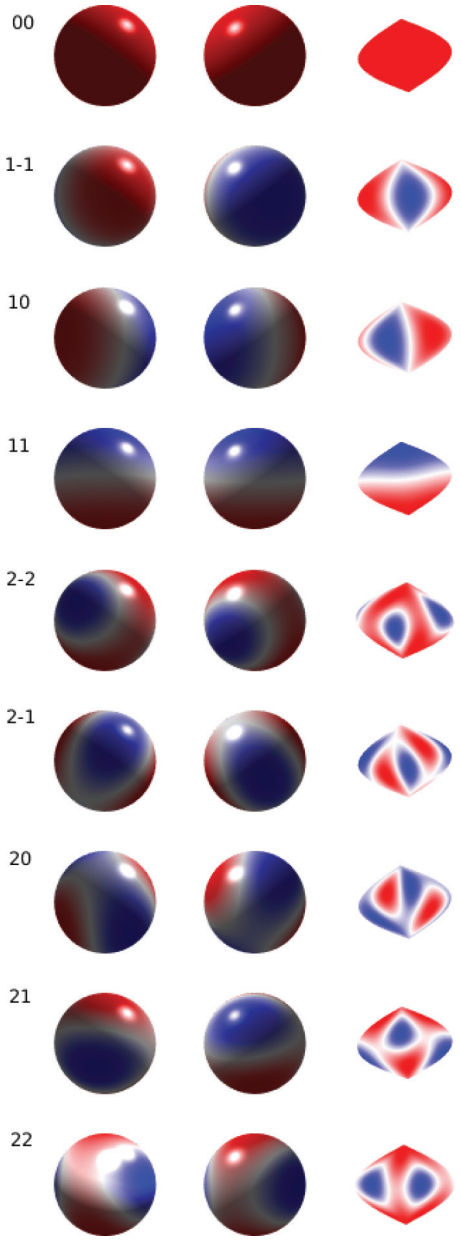

FIG. 4. NFT eigenmodes of the spherical brain hemisphere for the mode numbers ℓm labeled at the left of the first column. Red indicates positive eigenmode regions and blue indicates negative eigenmode regions. Nodal lines are shown in white. The first and second columns show lateral and medial views of modes on the spherical brain hemisphere. The third column shows a flattened projection of the modes so the whole surface is visible in a single view.

where the mode label η can be replaced by the paired indexes $\lambda\mu$ which correspond to the pair ℓm in the spherical case and $\phi_n(k_\eta, \omega) = y_\eta(\mathbf{r}_0)e^{i\omega t_{os}}e^{-\frac{1}{2}\omega^2 t_s^2}$.

We note a slight difference between the stimuli used in the analytical (on the sphere, as in [17]) and numerical methods. In the analytical methods, we use a narrow Gaussian in both space and time, but in the numerical methods, the stimulus is a δ function in position and Gaussian in time [17]. When discretized for numerical calculations, the former corresponds to a narrow rectangular profile that

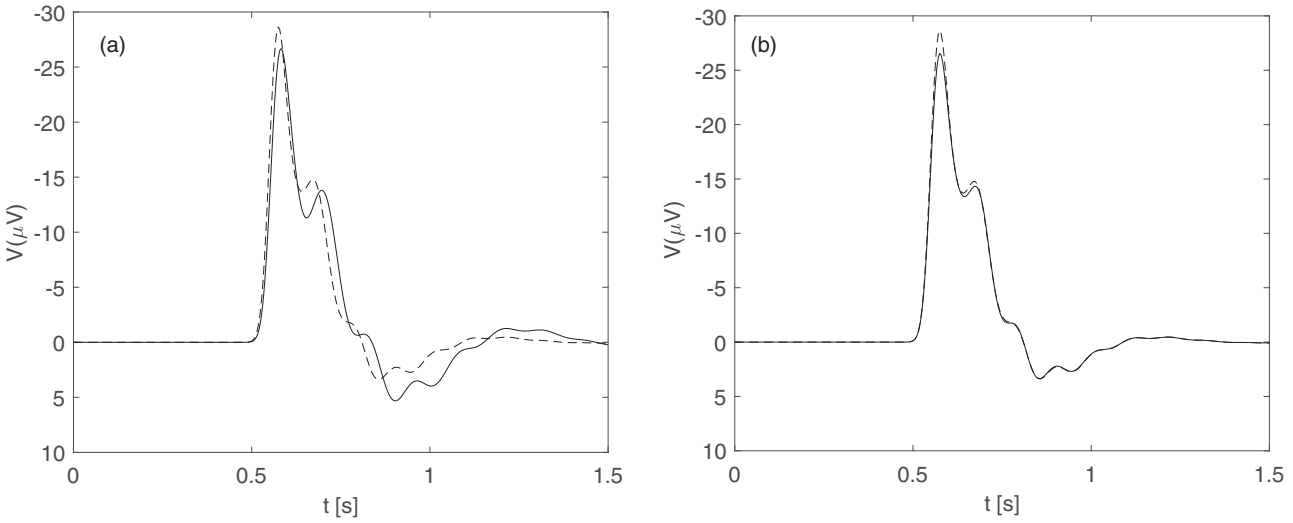

FIG. 5. ERP time series for the parameters in Table I. (a) Spherical cortex obtained from Eqs. (34) and (40) in the parietal lobe, where the solid line is computed analytically and the dashed line is computed numerically for a point where $\Delta\vartheta \approx 45^\circ$. (b) Convoluted cortex (solid line) and spherical cortex (dashed line) obtained from Eq. (40), both computed numerically for a point where $\Delta\vartheta \approx 45^\circ$.

covers one element of the discretized surface. In the numerics, we thus set the width of the analytic stimulus to $\theta_s = 0.3^\circ$ according to the approximation $\pi\theta_s^2 R_s^2 = A_{\rm tot}/N_p$, which makes the total impulse the same. Close to the stimulus point, the difference in profiles is expected to cause a slight difference in the ERP, but these should diminish rapidly with ϑ.

Because of the difference between the stimulus profile in the analytical and numerical methods, we adjust the normalization of the latter to best match the analytic one in the spherical case and retain that normalization in all other examples. Both sets of results are also multiplied by a constant factor such that outcomes match typical experimental ERP amplitudes (e.g., in μV) [2], as was done in [17].

III. RESULTS

Our recent work [17] explored and analyzed the modal form of ERPs in a spherical geometry using neural field theory for the parameters in Table I. In this section, we analyze and explore the modal form of ERPs in a single convoluted brain hemisphere. In this section, we compare ERP time series to determine how folding affects the results.

A. Eigenmodes of a single brain hemisphere

Previous work [13] derived NFT eigenmodes on the convoluted cortex and analyzed the activity eigenmodes on the brain hemisphere, which we reproduce in this section as a test of our code. For a sphere, the eigenvalues for a given ℓ are independent of m, but on the convoluted cortex, we expect this degeneracy to be lifted for individual μ at the same λ due to folding-induced splitting [13,18].

In Fig. 3, we show the spatial structure of the nine NFT eigenmodes on the convoluted cortex, where each eigenmode is labeled by λ and μ at the left. The $\lambda = 0$ eigenmode is uniform and there is no nodal line. For $\lambda = 1$, three eigenmodes exist that have enhanced activity in half of the brain hemisphere, while in the other half the activity is decreased, which is similar to the $\ell = 1$ spherical harmonics and reproduces them in the spherical limit. For the $\lambda = 2$ eigenmodes, the nodal lines intersect on the sphere and near intersections occur when the cortex is close to spherical, with very similar structure seen. Note that as time progresses, the positive and negative regions of all modes alternate in time, according to Eq. (40).

Figure 4 shows the first nine NFT eigenmodes on a spherical cortex. According to our prior work [13,18], each $\lambda\mu$ eigenmode is mainly a linear combination of the $Y_{\ell m}$ with $\ell = \lambda$. Accordingly, for the $\ell = 0$ eigenmode, we see the uniform Y_{00} mode with no nodal line. The $\ell = 1$ modes $Y_{\ell m}$ have one nodal line, with enhanced activity in one half of the surface and reduced activity in the other half, as for $\lambda = 1$. The $\ell = 2$ eigenmodes are also close to the $\lambda = 2$ eigenmodes, with more complex modal structure in which each mode $y_{\lambda\mu}$ is predominantly a superposition of the $Y_{\ell m}$ with $\ell = \lambda$ (see [13] for a detailed analysis). Thus our results are consistent with these eigenmodes being dominated by spherical harmonic components with $\ell = \lambda$, despite the folding of the convoluted cortex [13].

B. ERPs in spherical and convoluted cortex

In this section, we compare analytic and numerical ERPs in a spherical and convoluted cortex to verify their consistency for the parameters listed in Table I and set the correct normalization of the numerical result, given its somewhat different stimulus profile.

Figure 5(a) shows an example of an ERP time series on a spherical cortex obtained from Eqs. (34) and (40) for $\Delta\vartheta = 45^\circ$. In Fig. 5(a), the solid line shows the analytic result and the dashed line is for the numerically computed result. The analytic time series shows a sharp negative peak and the response onset is delayed with respect to the stimulus because of the $\sim$40 ms time taken to travel from thalamus to cortex [17]. The initial negative peak amplitude of around $-27\,\mu$V

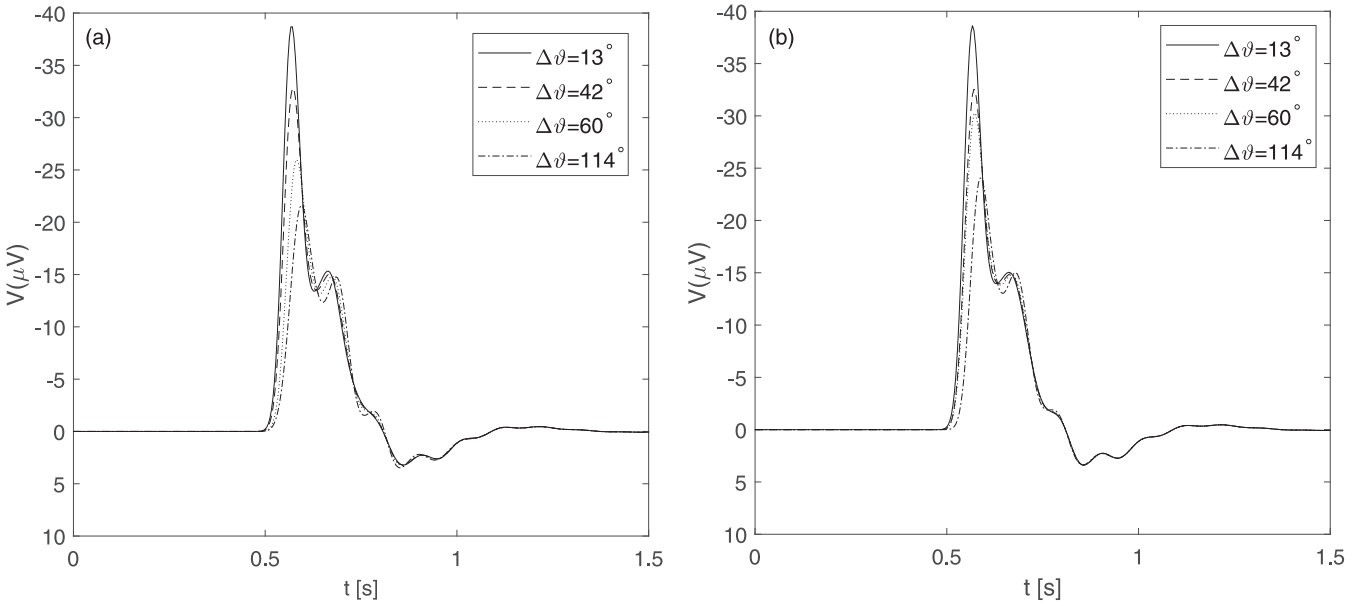

FIG. 6. ERP time series vs $\Delta\vartheta$, as indicated in the legend, for the parameters in Table I. (a) Convoluted cortex. (b) Spherical cortex.

rapidly decays with a decay time of ∼0.07 s. We observe a secondary peak at $t \simeq 0.70$ s with a negative amplitude of around -14 μV. After 0.70 s, we see that the ERP amplitude decays rapidly, and after 1.5 s, it is negligible. The numerical ERP time series from Eq. (40) also shows a sharp negative peak with initial amplitude -29 μV and decay time ∼0.07 s, a secondary peak at ≈0.70 s with negative amplitude of around -15 μV, followed by rapid decay. All features match to within a few μV, despite the slightly different stimulus profiles. Overall, the numerically computed ERP is slightly sharper than the analytical one, as expected because of the spatially smoother stimulus in the latter case.

In Fig. 5(b), we compare the ERP time series computed numerically in a convoluted cortex and spherical cortex for $\Delta\vartheta = 45^\circ$ to show the difference that can be caused by folding of the cortex, where $\Delta\vartheta$ is the distance between the stimulus point and the measurement point. Figure 5(b) shows examples of the ERP time series for the convoluted cortex and spherical cortex obtained from Eq. (40) for the parameters listed in Table I. We see a sharp negative peak for the convoluted cortex ERP, shown by the solid line, but smaller than for the spherical cortex. We observe an initial negative peak amplitude of around -27 μV, which rapidly decays with an initial decay time of 0.07 s with smaller amplitude than in the spherical cortex.

We see a shoulder on the peak at time 0.68 s with negative amplitude around -14.5 μV, which is also very similar to the spherical case [17]. After $t = 0.70$ s, the amplitude decays rapidly, in excellent agreement with spherical cortex, and after $t = 1.5$ s it is negligible.

C. Dependence on $\Delta\vartheta$

In this section, we explore the effect of $\Delta\vartheta$ (the coordinate difference between the stimulus point and measuring point on the cortex) on the ERP time series shown in Fig. 6 for the convoluted cortex and spherical cortex, respectively. From Fig. 6(a), we see that as $\Delta\vartheta$ varies from 13° to 114°, the maximum negative peak decreases significantly from around -39 to -22 μV and is delayed slightly from 0.57 to 0.59 s. In contrast, the secondary peak only decreases slightly in amplitude and has a nearly unchanged delay. Similarly, from Fig. 6(b) for a spherical cortex, we also observe that the negative peak decreases in size with increasing $\Delta\vartheta$; indeed, it decreases from around -38.6 to -24 μV, but is increasingly delayed, as in the convoluted cortex, as $\Delta\vartheta$ increases from 13° to 114°. The secondary peak only decreases in amplitude very slightly with ϑ and is delayed from -0.66 to -0.68 s.

Overall, we observe that with increasing $\Delta\vartheta$, the negative amplitude decreases monotonically and the ERP decreases with distance due to damping and spreading, which is in accord with our recent work [17]. A linear fit of the peak time vs $\Delta\vartheta$ yields phase velocities for the first and second peaks of 5 and 6 m s^{-1}, respectively, when translated to linear velocity on an equal area sphere via $v_p = R_s\Delta\vartheta/\Delta t$.

In the convoluted case, different measuring points with the same $\Delta\vartheta$ can have very different folding intervening between them and the stimulus point, as seen in Fig. 7, which shows the stimulus and measurement points at fixed $\Delta\vartheta$ on the

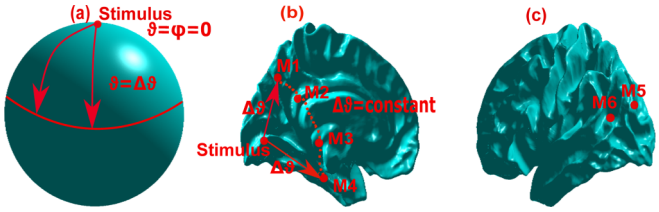

FIG. 7. Locus of constant $\Delta\vartheta$ in convoluted and spherical geometries. (a) Spherical cortex showing $\Delta\vartheta$. (b) Freesurfer convoluted cortical hemisphere showing stimulus point with different measuring points M1–M4 at constant distance $\Delta\vartheta$. (c) Lateral surface of the convoluted cortical hemisphere with measuring points M5 and M6, also at constant distance $\Delta\vartheta$.

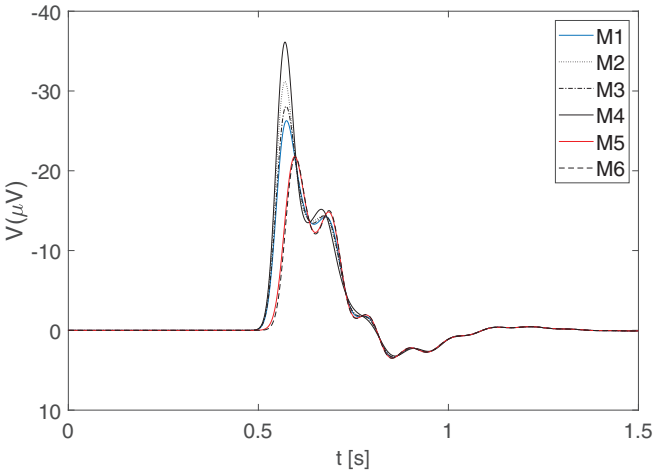

FIG. 8. ERP time series for uniform $\Delta\vartheta \approx 55^\circ$, for the parameters in Table I with different measurement points on the cortex, as indicated in the legend, where M1–M6 indicate the different measuring points from Fig. 7.

convoluted cortex and spherical cortex. In Fig. 8, we illustrate the effects of folding by examining ERPs at different locations M1–M6 with the same $\Delta\vartheta$. We observe that peak ERPs vary by roughly $\pm 25\%$ depending on the location of the measurement points, but all ERP amplitudes become increasingly similar at later times, a point we return to in Sec. III B, where we show that it is due to the dominance of the spatially uniform 00 mode. We see that in this case, activity at M1 and M5 or M6 is most dissimilar in terms of negative peak amplitude and has a slight difference in the peak time of 0.02 s. On the lateral surface of the cortex, we observe more visible sulci and gyrus.

D. Modal dynamics

Our recent work [17,20] showed that a handful of modes dominate ERPs. For this reason, next we explore the eigenmode structure of the ERP time series on a convoluted cortex and compare the results with our recent work [17], which analyzed the eigenmode structure of the ERP time series on a spherical cortex.

Figure 9 shows ERP activity at various times. At $t - t_s =$ 4 ms, the response is small and localized near $\mathbf{r}_0$ so no large-scale disturbance is seen. After that, we see that at $t - t_s =$ 44 ms, the response is intense around $\mathbf{r}_0$ and has started to spread over the hemisphere. The spreading at an approximate phase velocity of 2 m s^{-1} continues to $t - t_s \approx 74$ ms, after which the activity decays and becomes steadily more uniform due to the dominance of the global mode and consistent with the convergence of all time series to a common form at large t seen in Figs. 6 and 8. By $t - t_s = 356$ ms, there is negligible activity over the brain hemisphere. To show the relative contributions of the first few eigenmodes to the ERP, Fig. 10(a) first plots the ERP time series using Eq. (40) with $\lambda = 0$, $\mu = 0$. We observe that this component of the ERP is independent of $\Delta\vartheta$, due to $y_{00}(\vartheta, \varphi)$ being constant. The maximum negative peak occurs at time ~0.6 s,which is similar to Fig. 5(b) but smaller in amplitude. We also observe from

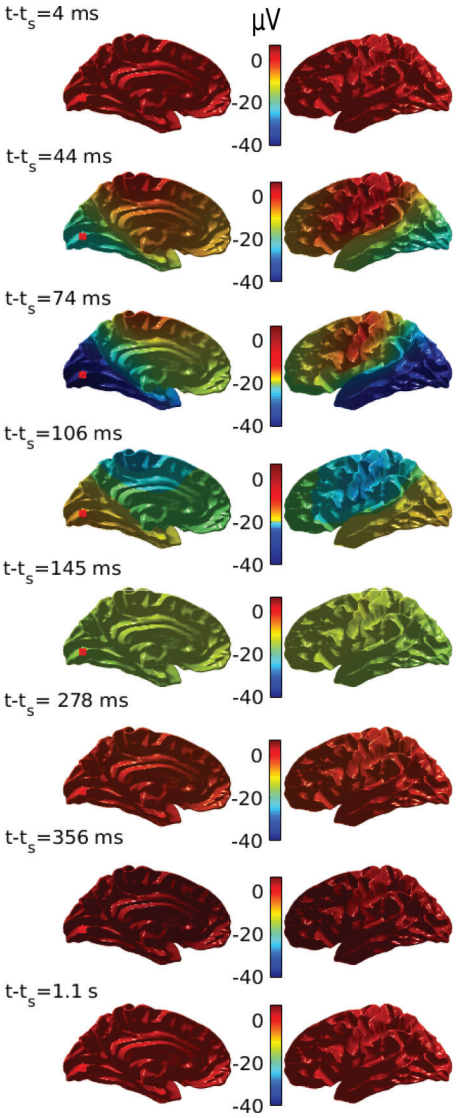

FIG. 9. Snapshots of ERP due to a stimulus at the red dot in a single brain hemisphere, showing spatial activity medial and lateral views as indicated by the color bars. Times are shown at left.

Fig. 10 that the $\lambda = 1$ modes peak near the main ERP peak and contribute to the maximum response. From Fig. 10(b) with $\lambda = 1$ and $\mu = -1$, we observe that the eigenmode has a smaller negative amplitude than the $\lambda = 0$, $\mu = 0$ mode, but is significant near the ERP peak. This mode also has more temporal oscillations and decays faster than the $\lambda = 0$, $\mu = 0$ mode. Figure 10(c) with $\lambda = 1$, $\mu = 0$ shows a smaller peak amplitude than Fig. 10(b) did for $\lambda = 1$, $\mu = -1$ and we observe that the peak amplitude is more damped than $\lambda = 0$, $\mu = 0$. Figure 10(d) is plotted for $\lambda = 1$, $\mu = 1$, where we observe a similar oscillating structure and rapid fall-off with time. Overall, Fig. 10 shows that the 00 mode dominates at long times, the other modes are most significant near the ERP peak, and the symmetry property of spherical eigenmodes $Y_{\ell m}(\vartheta, \varphi) = (-1)^\ell Y_{\ell m}(180^\circ - \vartheta, \varphi)$ and the resulting responses are approximately preserved for $\lambda = 0, 1$ on the convoluted cortex. To explore how ERP activity is dominated by low order modes, we next plot the contributions of

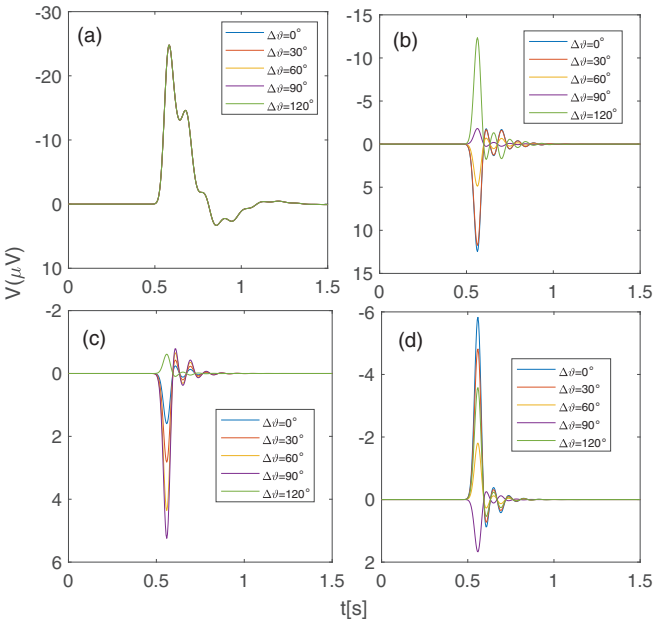

FIG. 10. Modal contributions to the numerically computed ERP time series on a convoluted cortex, plotted for different $\Delta\vartheta$, as indicated in the legend for the parameters in Table I and using Eq. (40). (a) $\lambda = 0$, $\mu = 0$ (all curves coincide due to this mode being uniform); (b) $\lambda = 1$, $\mu = -1$; (c) $\lambda = 1$, $\mu = 0$; (d) $\lambda = 1$, $\mu = 1$.

individual eigenmodes versus time in Fig. 11 at $\Delta\vartheta = 45^\circ$ using

$$\phi_e(\mathbf{r}, t) = \sum_{\lambda=0}^{\infty} \phi_e^{\lambda}(\mathbf{r}, t), \tag{41}$$

with

$$\phi_e^{\lambda}(\mathbf{r}, t) = \sum_{\mu=-\lambda}^{\lambda} y_{\lambda\mu}(\mathbf{r}) a_{\lambda\mu} e^{-i\omega_{\lambda\mu} t}. \tag{42}$$

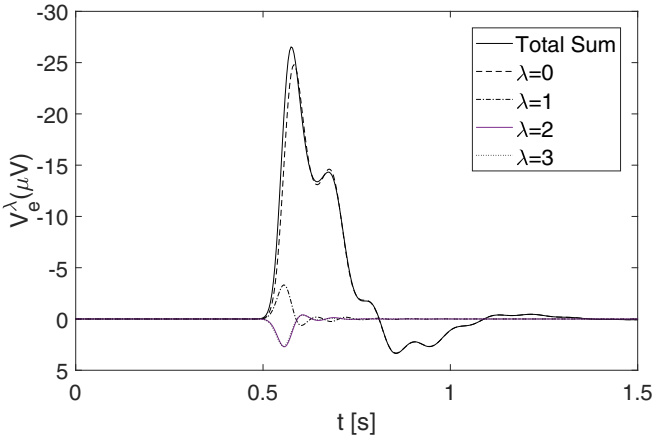

FIG. 11. Numerically computed contributions of various λ to the total ERP time series for the parameters in Table I from Eq. (40) for a convoluted cortex with $\Delta\vartheta = 45^\circ$. Here the total ERP and the time series of the ERP voltages V_e^{λ} that correspond to the ϕ_e^{λ} from Eq. (42) are shown, as indicated in the legend.

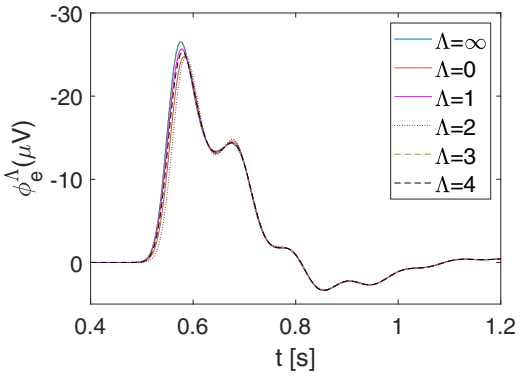

FIG. 12. Cumulative sums of numerically computed ERP contributions V_e^{λ} for a convoluted cortex and the parameters in Table I using Eq. (40) with $\Delta\vartheta = 45^\circ$. Here, the time series are plotted for sums over μ and $\lambda \leqslant \Lambda$, as in Eq. (43), with Λ indicated in the legend.

We observe that the series converges rapidly, with $\lambda > 0$ modes contributing chiefly near the primary ERP peak, then damping rapidly as time progresses, with the $\lambda = 0$ mode dominating at longer times. Further interpretation of this point is shown in Fig. 12, which shows total contributions to the ERP for $\lambda \leqslant \Lambda$ vs Λ, using the definition

$$\phi_e^{\Lambda}(\mathbf{r}, t) = \sum_{\lambda=0}^{\Lambda} \phi_e^{\lambda}(\mathbf{r}, t). \tag{43}$$

We observe that multiple modes are only significant near the ERP peak and retention of modes up to $\Lambda \approx 2$ (i.e., nine modes) is sufficient to represent the ERP activity to within 2–3 μV at all times in the example shown.

IV. SUMMARY AND CONCLUSION

We have used physiology-based neural field theory (NFT) on a convoluted cortex to explore modal effects on ERPs due to impulse stimuli. We numerically computed eigenmodes of the brain activity on a convoluted cortex and compared ERPs on a convoluted cortex, numerically and analytically, with cases on a corresponding spherical cortex.

NFT is used to calculate ERPs in the convoluted cortex and spherical cortex using Eqs. (34) and (40) via the NFT transfer function, with eigenmodes calculated numerically via the Helmholtz equation in the convoluted case. The key results are the following:

(i) The ERP time series are computed via analytic and numerical methods in a spherical brain cortex and a convoluted one. The two cases are very similar, but the peak is slightly sharper in the numerical case due to the difference in the detailed stimulus profile.

(ii) With increasing angle $\Delta\vartheta$ between the stimulus point and measuring point, the ERP peak falls off due to damping and spreading over the cortex. The velocity of the first peak is 5 m s^{-1} and that of the second peak is 6 m s^{-1}, which are consistent with typical experimental values. At fixed $\Delta\vartheta$, ERPs differ by up to $\pm 25\%$ between different measuring points at the same $\Delta\vartheta$ in the convoluted cortex due to folding.

(iii) The ERP activity is strongest near the stimulus location $\mathbf{r}_0$ and with time passing spreading through the whole cortex. With increasing time, activity decays until the 00 mode dominates, giving a uniform response across the whole cortex.

(iv) Just a few modes with $\lambda \leqslant \Lambda$ dominate the ERP activity. Indeed, the upper bound $\Lambda = 2$ is sufficient for the representation of the ERPs activity at $\Delta\vartheta = 45^\circ$, while $\Lambda = 0$ suffices except near the peak, and even there is semiquantitatively correct. Similarly, in recent numerical work [20], we found that just two modes sufficed to explain the main features of experimental ERPs driven by visual stimuli and the present analysis confirms that just a few modes are responsible for the main features of ERPs in a convoluted cortex.

Overall, there are strong similarities of ERPs to those seen in the spherical case; however, cortical folding has significant effects on eigenmodes and activity. In the future, this analysis on the convoluted cortex will be useful for more detailed and accurate comparison with experimental data than the spherical approximation.

ACKNOWLEDGMENTS

This work was supported by a University of Sydney International Scholarship, by the Australian Research Council Center of Excellence for Integrative Brain Function (ARC Grant No. CE140100007), and by the Australian Research Council Laureate Fellowship Grant No. FL140100025.

[1] C. J. Rennie, P. A. Robinson, and J. J. Wright, Biol. Cybern. **86**, 457 (2001).
[2] C. C. Kerr, C. J. Rennie, and P. A. Robinson, Biol. Cybern. **98**, 171 (2008).
[3] O. D. Creutzfeldt, S. Watanabe, and H. D. Lux, Electroencephalogr. Clin. Neurophysiol. **20**, 1 (1966).
[4] H. Davis, P. A. Davis, A. L. Loomis, E. N. Harvery, and G. Hovert, J. Neurophysiol. **2**, 500 (1939).
[5] C. C. Kerr, C. J. Rennie, and P. A. Robinson, J. Neurosci. Meth. **179**, 101 (2009).
[6] W. D. Penny, S. J. Kiebel, J. M. Kilner, and M. D. Rugg, Trends Neurosci. **25**, 387 (2002).
[7] D. M. Regan, Electroencephalogr. Clin. Neurophysiol. **20**, 238 (1989).
[8] G. Pfurtscheller and F. Lopes da Silva, Clin. Neurophysiol. **110**, 1842 (1999).
[9] J. Harsh, U. Voss, J. Hull, S. Schrepfer, and P. Badia, Psychophysiol. **31**, 244 (1994).
[10] C. C. Kerr, S. J. Van Albada, S. A. Neymotin, G. L. Chadderdon, P. A. Robinson, and W. W. Lytton, Front. Comput. Neurosci. **7**, 1 (2013).
[11] H. Nordby, K. Hugdahl, R. Stickgold, K. S. Bronnick, and J. A. Hobson, Neurorep. **7**, 1082 (1996).
[12] P. A. Robinson, P. N. Loxley, S. C. O'Connor, and C. J. Rennie, Phys. Rev. E **63**, 041909 (2001).
[13] P. A. Robinson, X. Zhao, K. M. Aquino, J. D. Griffiths, S. Sarkar, and G. Mehta-Pandejee, NeuroImage **142**, 79 (2016).
[14] K. N. Mukta, J. N. MacLaurin, and P. A. Robinson, Phys. Rev. E **96**, 052410 (2017).
[15] P. L. Nunez and L. Srinivasan, *Electric Fields of the Brain: The Neurophysics of EEG* (Oxford University Press, New York, 2006).
[16] P. L. Nunez, *Neocortical Dynamics and Human EEG Rhythms* (Oxford University Press, New York, 1995).
[17] K. N. Mukta, Xiao Gao, and P. A. Robinson, Phy. Rev. E **99**, 062304 (2019).
[18] N. C. Gabay and P. A. Robinson, Phys. Rev. E **96**, 032413 (2017).
[19] D. Bouattoura, P. Gaillard, P. Villon, and F. Langevin, Med. Biol. Eng. Comput. **36**, 415 (1998).
[20] P. A. Robinson, J. C. Pagès, N. C. Gabay, T. Babaie, and K. N. Mukta, Phys. Rev. E **97**, 042418 (2018).
[21] S. Visser, R. Nicks, O. Faugeras, and S. Coombes, Phys. D: Non. Phenom. **349**, 27 (2017).
[22] D. Daini, G. Ceccarelli, E. Cataldo, and V. Jirsa, Phys. Rev. E **101**, 012202 (2020).
[23] P. A. Robinson, C. J. Rennie, and D. L. Rowe, Phys. Rev. E **65**, 041924 (2002).
[24] P. A. Robinson, C. J. Rennie, and J. J. Wright, Phys. Rev. E **56**, 826 (1997).
[25] P. A. Robinson, C. J. Rennie, D. L. Rowe, and S. C. O'Connor, Hum. Brain Mapp. **23**, 53 (2004).
[26] C. C. Kerr, C. J. Rennie, and P. A. Robinson, Clin. Neurophysiol. **122**, 134 (2011).
[27] H. R. Wilson and J. D. Cowan, Kybernetik **13**, 55 (1973).
[28] W. J. Freeman, *Mass Action in the Nervous System* (Academic, New York, 1975).
[29] F. H. Lopes da Silva, A. Hoeks, H. Smits, and L. H. Zetterberg, Kybernetik **15**, 27 (1974).
[30] C. J. Rennie, P. A. Robinson, and J. J. Wright, Phys. Rev. E **59**, 3320 (1999).
[31] D. L. Rowe, P. A. Robinson, and C. J. Rennie, J. Theor. Biol. **231**, 413 (2004).
[32] P. A. Robinson, C. J. Rennie, D. L. Rowe, S. C. O'Connor, and E. Gordon, Philos. Trans. R. Soc. B. **360**, 1043 (2005).
[33] M. S. Zobaer, R. M. Anderson, C. C. Kerr, P. A. Robinson, K. K. H. Wong, and A. L. D'Rozario, Biol. Cybern. **111**, 149 (2017).
[34] V. Braitenberg and A. Schüz, *Cortex: Statistics and Geometry of Neuronal Connectivity* (Springer, Berlin, 1998).
[35] O. Calin, D. C. Chang, K. Furutani, and C. Wasaki, The eigenfunction expansion method, in *Heat Kernels for Elliptic and Sub-elliptic Operators*, Applied and Numerical Harmonic Analysis (Birkhäuser, Boston, 2011).
[36] C. Constanda, The method of eigenfunction expansion, in *Solution Techniques for Elementary Partial Differential Equations* (Taylor and Francis, New York, 2016), Chap. 7.
[37] B. Fischl, M. I. Sereno, and A. M. Dale, NeuroImage **9**, 195 (1999).